INTERNATIONAL JOURNAL FOR NUMERICAL METHODS IN FLUIDS, VOL. 8, 913–931 (1988)

PREDICTION OF OSCILLATING THICK CAMBERED AEROFOIL AERODYNAMICS BY A LOCALLY ANALYTIC METHOD

HSIAO-WEI D. CHIANG AND SANFORD FLEETER

Thermal Sciences and Propulsion Center, School of Mechanical Engineering, Purdue University, West Lafayette, Indiana 47907, U.S.A.

SUMMARY

A complete first-order model and locally analytic solution method are developed to analyse the effects of mean flow incidence and aerofoil camber and thickness on the incompressible aerodynamics of an oscillating aerofoil. This method incorporates analytic solutions, with the discrete algebraic equations which represent the differential flow field equations obtained from analytic solutions in individual grid elements. The velocity potential is separated into steady and unsteady harmonic parts, with the unsteady potential further decomposed into circulatory and non-circulatory components. These velocity potentials are individually described by Laplace equations. The steady velocity potential is independent of the unsteady flow field. However, the unsteady flow is coupled to the steady flow field through the boundary conditions on the oscillating aerofoil. A body-fitted computational grid is then utilized. Solutions for both the steady and the coupled unsteady flow fields are obtained by a locally analytic numerical method in which locally analytic solutions in individual grid elements are determined. The complete flow field solution is obtained by assembling these locally analytic solutions. This model and solution method are shown to accurately predict the Theodorsen oscillating flat plate classical solution. Locally analytic solutions for a series of Joukowski aerofoils demonstrate the strong coupling between the aerofoil unsteady and steady flow fields, i.e. the strong dependence of the oscillating aerofoil aerodynamics on the steady flow effects of mean flow incidence angle and aerofoil camber and thickness.

KEY WORDS Unsteady aerodynamics Aeroelasticity Flutter Propulsion Flow-induced vibration

INTRODUCTION

To predict the susceptibility to flutter, the unsteady aerodynamic forces and moments acting on a harmonically oscillating aerofoil must be determined. This enables the unsteady aerodynamic work being fed into the aerofoil to be calculated and an assessment made as to whether this is sufficient to overcome the available mechanical damping.

The methods currently in use for this unsteady aerodynamic calculation are two-dimensional and based on thin aerofoil theory. Typically, flat plate aerofoils with no thickness at zero incidence to a mean uniform and parallel steady flow are considered. The unsteady flow field is completely uncoupled from the uniform steady flow by considering the unsteady aerodynamics due to the oscillating aerofoil to be a small perturbation to the uniform parallel steady flow. The linearized unsteady flow field is then calculated using conformal mapping techniques and circulation theory.

0271–2091/88/080913–19$09.50

Received 1 December 1986
Revised 26 October 1987

In many applications, however, aerofoils with non-zero mean incidence, arbitrary shape and large camber must be considered. Horlock[1] extended the approach of Sears[2] to consider a flat plate aerofoil at small angle of attack. Naumann and Yeh[3] extended Horlock's analysis to consider a thin aerofoil with constant small camber. These analyses showed that the unsteady aerodynamic forces acting on an aerofoil were affected by both the small incidence angle and the small aerofoil camber. However, Horlock neglects second-order terms, following Sears, and also assumes a small angle of attack. Thus these results are approximate and cannot be extended to finite incidence angles or large camber. The analysis of Goldstein and Atassi[4] for thin lifting aerofoils subject to a periodic gust showed the inaccuracy of Horlock's unsteady lift result.

Atassi and Akai[5] developed an analysis for moderate-camber aerofoils in cascade oscillating in a uniform incompressible flow field. In the complex plane two singular integral equations are obtained for the density distribution of singularities along the aerofoil contours and wakes. These equations are coupled through the Kutta condition, with the use of a numerical integral solution procedure.

All of the above noted incompressible harmonic unsteady aerodynamic analyses utilize classical aerofoil techniques or extensions thereof. This results in solutions in the form of integral equations, with the determination of general analytical solutions a formidable mathematical task. Although such classical models and integral solution techniques are of value, numerical techniques permit the mathematical modelling of the flow physics to be extended and significantly enhanced. However, even though numerical methods have been developed and utilized to predict steady aerofoil flow fields with impressive results, relatively less interest has been shown in developing and applying numerical methods to unsteady flows.

In this paper a complete first-order mathematical model is developed to analyse the effects of mean flow incidence and aerofoil camber and thickness on the inviscid incompressible aerodynamics of a harmonically oscillating aerofoil. Also, a locally analytic solution method is developed for both the unsteady and the steady flow fields. In this method analytic solutions in individual grid elements are determined, with the complete flow field solution obtained by assembly of these locally analytic solutions.

A velocity potential formulation is utilized for the mathematical model. The velocity potential is separated into steady and unsteady harmonic parts, with the unsteady potential further decomposed into circulatory and non-circulatory components. These velocity potentials are individually described by Laplace equations. The steady velocity potential is independent of the unsteady flow field. However, the unsteady flow is coupled to the steady flow field through the boundary conditions on the surfaces of the oscillating aerofoil.

The various numerical methods utilized to solve partial differential equations are distinguished from one another by the means used to derive the corresponding algebraic representation of the differential equations. In finite difference methods Taylor series expansion and control volume formulations are most often used. For finite element methods variational formulations and the method of weighted residuals are employed. In the locally analytic method the discrete algebraic equations are obtained from the analytical solution in each local grid element.

The concept of locally linearized solutions was applied to the problem of the steady inviscid transonic flow past thin aerofoils by Spreiter *et al.*[6-8] and subsequently extended to oscillating aerofoils in transonic flow by Stahara and Spreiter.[9] Also Dowell[10] developed a rational approximate method for unsteady transonic flow which is broadly related to the local linearization concept. The locally analytic method for steady two-dimensional fluid flow and heat transfer problems was initially developed by Chen *et al.*[11-14] They have shown that the locally analytic method has several advantages over the finite difference and finite element methods. In particular, it is less dependent on grid size and the system of algebraic equations is relatively

stable. Also, since the solution is analytic, it is differentiable in any direction and is a continuous function in the solution domain. The disadvantage of the local analytic method is that, as will be seen, mathematical analysis is required before programming.

MATHEMATICAL MODEL

The two-dimensional flow past a thick cambered aerofoil executing torsion mode oscillations together with the non-dimensional Cartesian co-ordinate system is schematically depicted in Figure 1. The steady and uniform far-field flow is specified by the velocity vector $\mathbf{U}_\infty$, with the mean incidence angle to the aerofoil, α_0, specified by the chordwise and normal far-field velocity components, U_∞ and V_∞.

For an incompressible inviscid fluid, a velocity potential function can be defined. The complete flow field is then described by a Laplace equation:

$$\nabla^2\Phi = 0, \tag{1}$$

where $\Phi = \Phi(X, Y, t)$ is the velocity potential.

The Laplace equation is linear. Thus the velocity potential can be decomposed into components by the superposition principle. In particular, the velocity potential is decomposed into steady and unsteady components, $\Phi_0(X, Y)$ and $\Phi'(X, Y, t)$. The unsteady potential is assumed to have a harmonic time dependence of frequency ω and is further decomposed into non-circulatory and circulatory components, $\Phi'_{NC}(X, Y)$ and $\Phi'_C(X, Y)$:

$$\Phi(X, Y, t) = \Phi_0(X, Y) + e^{ikt}[\Phi'_{NC}(X, Y) + \Gamma'\Phi'_C(X, Y)], \tag{2}$$

where $\nabla^2\Phi_0 = 0$, $\nabla^2\Phi'_{NC} = 0$, $\nabla^2\Phi'_C = 0$, Γ' is the unknown unsteady flow circulation and k is the reduced frequency, $k = \omega b/U_\infty$.

To complete the mathematical model, far-field, aerofoil surface and wake-dividing streamline boundary conditions must be specified for the three velocity potential functions $\Phi_0(X, Y)$, $\Phi'_{NC}(X, Y)$ and $\Phi'_C(X, Y)$.

In the far field the flow is steady and uniform. Hence both the oscillatory component of the solution and the unsteady circulation vanish in the far field. Thus the velocity potential boundary conditions are as given in equation (3). It should be noted that, for a flat plate or symmetric aerofoil at zero incidence, the steady circulation Γ is zero.

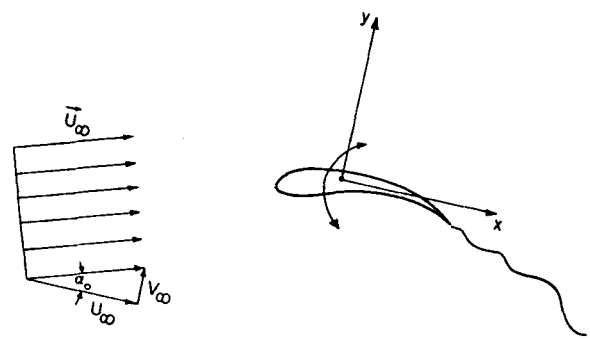

Figure 1. Schematic of the flow field

$$\Phi_0|_{\text{far field}} = U_\infty X + V_\infty Y + \Gamma\Theta/2\pi, \tag{3a}$$

$$\Phi'_{NC}|_{\text{far field}} = 0, \tag{3b}$$

$$\Phi'_C|_{\text{far field}} = 0, \tag{3c}$$

where Γ is the unknown steady flow circulation and Θ is the standard polar co-ordinate.

The aerofoil surface boundary conditions specify that the normal velocity of the flow field is equal to that of the aerofoil:

$$\left.\frac{\partial \Phi_0}{\partial n}\right|_{\text{aerofoil}} = 0 \tag{4a}$$

$$\left.\frac{\partial \Phi'_C}{\partial n}\right|_{\text{aerofoil}} = 0 \tag{4b}$$

$$\left.\frac{\partial \Phi'_{NC}}{\partial n}\right|_{\text{aerofoil}} = W'(X, Y) = \text{upwash}, \tag{4c}$$

where n denotes the surface unit normal.

The upwash on the aerofoil, $W'(X, Y)$, is a function of both the position of the aerofoil and the steady flow field. Thus it is this boundary condition which couples the unsteady flow field to the steady aerodynamics. For an aerofoil executing harmonic torsion mode oscillations about an elastic axis location at X_0 as measured from the leading edge, the upwash on the surfaces of the aerofoil is defined by

$$W'(X, Y) = \bar{\alpha}\left(\frac{ik[(X - X_0) + Y(\partial f/\partial X)] + U_0 + V_0(\partial f/\partial X)}{[1 + (\partial f/\partial X)^2]^{1/2}} + \frac{(\partial U_0/\partial Y)[(X - X_0)\partial f/\partial X + Y]}{[1 + (\partial f/\partial X)^2]^{1/2}} - \frac{(\partial V_0/\partial Y)[(X - X_0) - Y(\partial f/\partial X)]}{[1 + (\partial f/\partial X)^2]^{1/2}}\right), \tag{5}$$

where $U_0 = U_0(X, Y)$ and $V_0 = V_0(X, Y)$ are the steady chordwise and normal velocity components determined from the solution for the steady velocity potential $\Phi_0(X, Y)$, $f(X)$ denotes the aerofoil profile and $\bar{\alpha}$ is the amplitude of the torsional oscillations.

The steady and unsteady velocity potentials are both discontinuous along the aerofoil wake-dividing streamline. The steady flow discontinuity is equal to the steady circulation Γ:

$$\Delta\Phi_0|_{\text{wake}} = \Phi_0^+ - \Phi_0^- = \Gamma = \Delta\Phi_0|_{\text{TE}}, \tag{6}$$

where TE denotes the aerofoil trailing edge and the superscripts + and − denote the upper and lower aerofoil surfaces respectively.

The unsteady flow discontinuity is satisfied with a continuous non-circulatory velocity potential and a discontinuous circulatory velocity potential. The circulatory velocity potential discontinuity is specified by requiring the pressure to be continuous across the wake and then utilizing the unsteady Bernoulli equation to relate the velocity potential and the pressure. For harmonic torsion mode aerofoil oscillations, the resulting circulatory potential wake streamline discontinuity is given in equation (7). Also specified is the continuity of the non-circulatory velocity potential along the wake streamline.

$$\Delta\Phi'_C|_{\text{wake}} = e^{-ik(X-1)}, \tag{7a}$$

$$\Delta\Phi'_{NC}|_{\text{wake}} = 0. \tag{7b}$$

In addition, the Kutta condition is applied to both the steady and the unsteady flow fields. This enables the steady and unsteady circulation constants, Γ and Γ', to be determined. For the steady flow field, the Kutta condition is satisfied by requiring the chordwise velocity components on the upper and lower aerofoil surfaces to be equal in magnitude at the trailing edge:

$$|U^{+}_{0\mathrm{TE}}| = |U^{-}_{0\mathrm{TE}}|. \tag{8}$$

The Kutta condition is imposed on the unsteady flow field by requiring no unsteady pressure difference across the aerofoil chordline at the trailing edge. The corresponding relation for the trailing-edge unsteady velocity potential difference is determined from the unsteady Bernoulli equation:

$$\Delta P'|_{\mathrm{TE}} = P'^{+}|_{\mathrm{TE}} - P'^{-}|_{\mathrm{TE}} = 0, \tag{9a}$$

$$(\nabla\Phi_0 \cdot \nabla\Phi' + ik\Phi')^{+}|_{\mathrm{TE}} = (\nabla\Phi_0 \cdot \nabla\Phi' + ik\Phi')^{-}|_{\mathrm{TE}}. \tag{9b}$$

The unsteady dependent variable of primary interest is the unsteady pressure. This is determined from the solution for the steady flow field, the unsteady velocity potential and the unsteady Bernoulli equation. Also, the unsteady aerofoil surface boundary conditions were applied on the mean position of the aerofoil (equation (5)). After transfer to the instantaneous aerofoil position,

$$P' = -\nabla\Phi_0 \cdot \nabla\Phi' - ik\Phi' + \frac{\partial U_0}{\partial Y}(-U_0 X + V_0 Y) - \frac{\partial V_0}{\partial Y}(V_0 X + U_0 Y), \tag{10}$$

where $U_0(X, Y)$ and $V_0(X, Y)$ are the chordwise and normal steady velocity components and the last two terms account for the transfer of the pressure value from the mean position of the aerofoil to its instantaneous position.

COMPUTATIONAL DOMAIN

Computational grid

The boundary-fitted computational grid developed by Thompson *et al.*[15] is utilized for the numerical solution because of its general availability. This method permits grid points to be specified along the entire boundary of the computational plane. As depicted in Figure 2, the boundary in the physical plane is denoted by the curve abcdefghia and encompasses the aerofoil, its wake and the far field. The application of this grid generation technique results in a smoothly spaced, non-overlapping grid at the interior points in the transformed (ξ, η) plane. A typical boundary-fitted grid for a Joukowski aerofoil is shown in Figure 3.

Laplace equations describe the complete flow field including the unknown velocity potentials Φ_0, Φ'_{NC} and Φ'_{C} (equation (2)). In the transformed (ξ, η) co-ordinate system the Laplace equation takes the following non-homogeneous form:

$$\frac{\partial^2\bar{\Phi}}{\partial\xi^2} + \alpha\frac{\partial^2\bar{\Phi}}{\partial\eta^2} - 2\alpha\beta\frac{\partial\bar{\Phi}}{\partial\eta} - 2\gamma\frac{\partial\bar{\Phi}}{\partial\xi} = F(\xi, \eta), \tag{11}$$

where $\bar{\Phi}$ is a shorthand method of writing these three velocity potentials in the transformed plane, i.e. $\bar{\Phi}$ denotes $\Phi_0(\xi, \eta)$, $\Phi'_{\mathrm{NC}}(\xi, \eta)$ or $\Phi'_{\mathrm{C}}(\xi, \eta)$; $F(\xi, \eta)$ contains the cross-derivative term $\partial^2\bar{\Phi}/\partial\xi\partial\eta$ and the coefficients α, β and γ are functions of the transformed co-ordinates ξ and η which are treated as constants in each individual grid element.

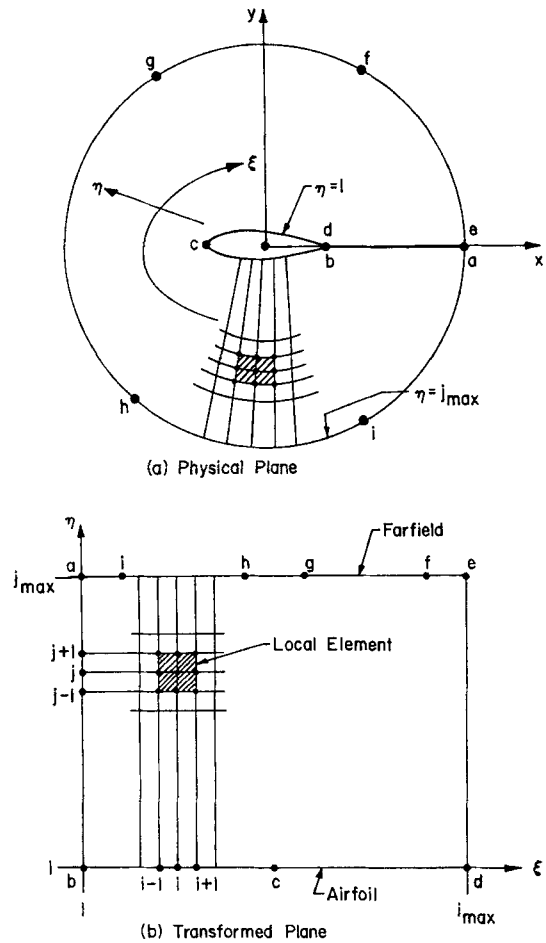

Figure 2. Body-fitted co-ordinate transformation

Analytic solution

To obtain the analytic solution to the transformed Laplace equation, it is first rewirtten as a homogeneous equation by defining a new dependent variable $\hat{\Phi}(\xi, \eta)$:

$$\frac{\partial^2\hat{\Phi}}{\partial\xi^2}+\alpha\frac{\partial^2\hat{\Phi}}{\partial\eta^2}-(\gamma^2+\alpha\beta^2)\hat{\Phi}=0, \tag{12}$$

where

$$\bar{\Phi}=\hat{\Phi}\exp(\gamma\xi+\beta\eta)-\frac{F(\gamma\xi+\beta\eta)}{2(\gamma^2+\alpha\beta^2)}.$$

The general solution for $\hat{\Phi}$ is determined by separation of variables and is given by

$$\hat{\Phi}(\xi,\eta)=[A_1\cos(\lambda\xi)+A_2\sin(\lambda\xi)][B_1\cosh(\mu\eta)+B_2\sinh(\mu\eta)], \tag{13}$$

where $\mu=[(\gamma^2+\alpha\beta^2+\lambda^2)/\alpha]^{1/2}$ and λ, A_1, A_2, B_1 and B_2 are constants to be determined from the boundary conditions.

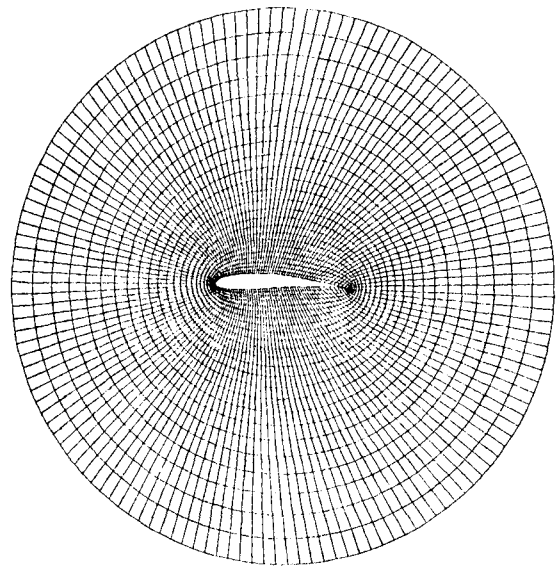

Figure 3. Body-fitted computational grid for a Joukowski aerofoil

LOCALLY ANALYTIC METHOD

In the locally analytic method analytic solutions of the partial differential equations are incorporated into the numerical technique. Analytic solutions in individual computational grid elements are determined by applying proper boundary conditions on each element to evaluate the unknown constants in the general velocity potential solution specified in equation (13). The solution to the global problem is then determined through the application of the global boundary conditions and the assembly of the locally analytic solutions.

Grid element boundary conditions

A typical computational grid element is schematically depicted in Figure 4. The local element boundary conditions specify the values of the various velocity potentials at the eight boundary nodal points. However, to obtain unique analytic solutions to the Laplace equation in this element, i.e. to determine the values of the integration constants in the general solution for each element, continuous boundary conditions are required on all four boundaries. For numerical purposes, these boundary conditions are expressed in an implicit formulation in terms of the three known nodal values on each element boundary. In particular, a combination of a linear and an exponential function are utilized on each boundary as they satisfy the Laplace equation:

$$\hat{\Phi}(\xi, 1) = a_1^{(1)} e^{\xi} + a_2^{(1)} \xi + a_3^{(1)}, \tag{14a}$$

$$\hat{\Phi}(1, \eta) = a_1^{(2)} e^{\eta} + a_2^{(2)} \eta + a_3^{(2)}, \tag{14b}$$

$$\hat{\Phi}(\xi, -1) = a_1^{(3)} e^{\xi} + a_2^{(3)} \xi + a_3^{(3)}, \tag{14c}$$

$$\hat{\Phi}(-1, \eta) = a_1^{(4)} e^{\eta} + a_2^{(4)} \eta + a_3^{(4)}, \tag{14d}$$

where the constants $a_1^{(i)}$, $a_2^{(i)}$ and $a_3^{(i)}$ are determined from the known values at the three nodal points on each boundary.

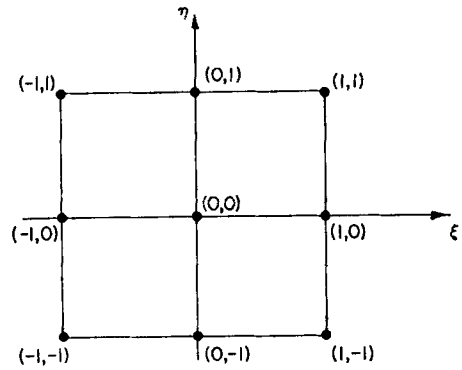

Figure 4. Local computational grid element

Locally analytic solution

The general analytic solution to the Laplace equation given in (13) is valid in individual grid elements as well as over the complete flow region. To determine the relationship between the velocity potential at the center of the typical grid element (Figure 4) and its surrounding values, the superposition principle is used to decompose the solution for $\hat{\Phi}$ into four components, each having only the non-homogeneous boundary condition:

$$\hat{\Phi}(\xi,\eta)=\sum_{n=1}^{\infty}\{A_{n_1}\sinh[\mu_n(\eta+1)]\sin[\lambda_n(\xi+1)]+A_{n_2}\sinh[\mu_n(\eta-1)]\sin[\lambda_n(\xi+1)]$$
$$+A_{n_3}\sinh[\mu'_n(\xi+1)]\sin[\lambda_n(\eta+1)]+A_{n_4}\sinh[\mu'_n(\xi-1)]\sin[\lambda_n(\eta+1)]\},\qquad(15)$$

where

$$\lambda_n=n\pi/2,\qquad \mu_n=[(\gamma^2+\beta^2\alpha+\lambda_n^2)/\alpha]^{1/2},\qquad \mu'_n=(\gamma^2+\beta^2\alpha+\lambda_n^2\alpha)^{1/2}.$$

The application of the local boundary conditions (equation (14)) together with the orthogonality of the Fourier series leads to the following values for A_{ni}:

$$A_{n_i}=C_{1n_i}\Phi(1,1)+C_{2n_i}\hat{\Phi}(1,0)+C_{3n_i}\hat{\Phi}(1,-1)+C_{4n_i}\hat{\Phi}(0,-1)$$
$$+C_{5n_i}\hat{\Phi}(-1,-1)+C_{6n_i}\hat{\Phi}(-1,0)+C_{7n_i}\hat{\Phi}(-1,1)+C_{8n_i}\hat{\Phi}(0,1),\qquad(16)$$

where the constants $C_{1n_i},\ldots,C_{8n_i}$ are functions of the $a_1^{(i)}$, $a_2^{(i)}$ and $a_3^{(i)}$ boundary constants.

With the analytic solution in an individual grid element thus specified (equations (15) and (16)), the value of $\hat{\Phi}$ at the centre of the element can be written as

$$\hat{\Phi}(0,0)=\sum_{n=1}^{\infty}\{[(A_{n_1}-A_{n_2})\sinh(\mu_n)+(A_{n_3}-A_{n_4})\sinh(\mu'_n)]\sin(\lambda_n)\}.\qquad(17)$$

Substituting for the A_{n_i} terms (equation (16)) leads to

$$\hat{\Phi}(0,0)=C'_1\hat{\Phi}(1,1)+C'_2\hat{\Phi}(1,0)+C'_3\hat{\Phi}(1,-1)+C'_4\hat{\Phi}(0,-1)$$
$$+C'_5\hat{\Phi}(-1,-1)+C'_6\hat{\Phi}(-1,0)+C'_7\hat{\Phi}(-1,1)+C'_8\hat{\Phi}(0,1),\qquad(18)$$

where the constants $C'_1, C'_2,\ldots,C'_8$ are functions of the $a_1^{(i)}$, $a_2^{(i)}$ and $a_3^{(i)}$ boundary constants as well as the transformed co-ordinate functions α, β and γ.

This solution for $\hat{\Phi}$ at the centre point is rewritten in term of the original dependent variable Φ as

$$\bar{\Phi}(0,0)=C_1\bar{\Phi}(1,1)+C_2\bar{\Phi}(1,0)+C_3\bar{\Phi}(1,-1)+C_4\bar{\Phi}(0,-1)$$
$$+C_5\bar{\Phi}(-1,-1)+C_6\bar{\Phi}(-1,0)+C_7\bar{\Phi}(-1,1)+C_8\bar{\Phi}(0,1), \quad (19)$$

where the constants $C_1, C_2, \ldots, C_8$ are again functions of the $a_1^{(i)}$, $a_2^{(i)}$ and $a_3^{(i)}$ boundary constants as well as the transformed co-ordinate functions α, β and γ.

Thus, the local analytic algebraic equation relating the value of the velocity potential at the centre of the computational element to its neighboring eight known nodal values has been completely determined.

Computational procedure

The above technique is applied to adjacent grid elements, with the boundary nodal point considered as the interior point. For a general grid element with centre at (i, j), the resulting algebraic relation between the centre value of the velocity potential and its eight surrounding nodal values is given by

$$\bar{\Phi}(i,j)=C_{i+1,j+1}\bar{\Phi}(i+1,j+1)+C_{i+1,j}\bar{\Phi}(i+1,j)+C_{i+1,j-1}\bar{\Phi}(i+1,j-1)+C_{i,j-1}\bar{\Phi}(i,j-1)$$
$$+C_{i-1,j-1}\bar{\Phi}(i-1,j-1)+C_{i-1,j}\bar{\Phi}(i-1,j)+C_{i-1,j+1}\bar{\Phi}(i-1,j+1)+C_{i,j+1}\bar{\Phi}(i,j+1), \quad (20)$$

where $2\leqslant i\leqslant i_{\max}-1$, $2\leqslant j\leqslant j_{\max}-1$ and C_{ij} are functions of the $a_1^{(i)}$, $a_2^{(i)}$ and $a_3^{(i)}$ boundary constants as well as the transformed co-ordinate functions α, β and γ.

The global boundary conditions are specified by

$$\bar{\Phi}(i,1)|_{\text{aerofoil surface}}=\text{upwash}, \qquad 1\leqslant i\leqslant i_{\max}, \quad (21a)$$
$$\bar{\Phi}(i,j_{\max})|_{\text{far field}}=\text{free stream}, \qquad 1\leqslant i\leqslant i_{\max}, \quad (21b)$$
$$\bar{\Phi}(i_{\max},j)|_{\text{wake}}=\text{upper wake}, \qquad 1<j<j_{\max}, \quad (21c)$$
$$\bar{\Phi}(1,j)|_{\text{wake}}=\text{lower wake}, \qquad 1<j<j_{\max}. \quad (21d)$$

The global boundary conditions together with the interior point solution specified in equation (20) for $\bar{\Phi}(i,j)$, where $2\leqslant i\leqslant i_{\max}-1$ and $2\leqslant j\leqslant j_{\max}-1$, lead to a system of algebraic equations. For a fixed j value,

$$-C_{i-1,j}\bar{\Phi}(i-1,j)+\bar{\Phi}(i,j)-C_{i+1,j}\bar{\Phi}(i+1,j)$$
$$=C_{i+1,j+1}\bar{\Phi}(i+1,j+1)+C_{i-1,j+1}\bar{\Phi}(i-1,j+1)+C_{i,j+1}\bar{\Phi}(i,j+1)$$
$$+C_{i+1,j-1}\bar{\Phi}(i+1,j-1)+C_{i-1,j-1}\bar{\Phi}(i-1,j-1)+C_{i,j-1}\bar{\Phi}(i,j-1). \quad (22)$$

The right-hand side of this equation is comprised of known quantities, i.e. the $(j-1)$ terms are known from the boundary conditions $(j=2)$ or the last sweep, with the $(j+1)$ terms determined from the boundary condition $(j=j_{\max}-1)$ or the previous iteration.

Equation (22) can be written as a tridiagonal matrix, with the matrix solved by the Thomas algorithm for all j values $(2\leqslant j\leqslant j_{\max}-1)$. This procedure is then iterated by successive over-relaxation until the entire solution converges.

MODEL AND SOLUTION VERIFICATION

To verify this mathematical model and locally analytic solution as well as to demonstrate the effects of grid refinement, predictions at zero incidence with a reduced frequency of 0·8 and a mid-chord elastic axis location are correlated with (1) Theodorsen's classical solution[16] for a flat plate aerofoil and (2) the solution of Atassi and Akai[5] for a Joukowski aerofoil with 11·25% thickness

and 3·5% camber. The excellent correlation obtained for these two verification cases is shown in Figures 5 and 6, which present the chordwise distributions of the complex unsteady pressure difference across the chordline of the oscillating flat plate and the Joukowski aerofoil respectively. In addition, the effect of grid refinement on the locally analytic predictions is demonstrated in Figure 6 for the oscillating Joukowski aerofoil. In particular, this figure also presents locally analytic predictions obtained on both a 140×25 and a 100×25 computational grid. As seen, there are only minimal differences between the two predictions.

RESULTS

This flow model and locally analytic solution are utilized to investigate the effects of aerofoil thickness and camber as well as mean flow incidence angle on both the steady and unsteady harmonic oscillating aerofoil aerodynamics. This is accomplished by considering a series of Joukowski aerofoils with elastic axis located at mid-chord and a value of 0·8 for the reduced frequency. The time required for a typical case is of the order of 350 CPU seconds on a Cyber 205 vector processing computer.

Thickness effects

The effects of aerofoil thickness on the steady and oscillating aerofoil aerodynamics are investigated by considering three uncambered Joukowski aerofoils with thickness-to-chord ratios of 10%, 25% and 40% (Figure 7). For comparison purposes, a flat plate aerofoil is also considered.

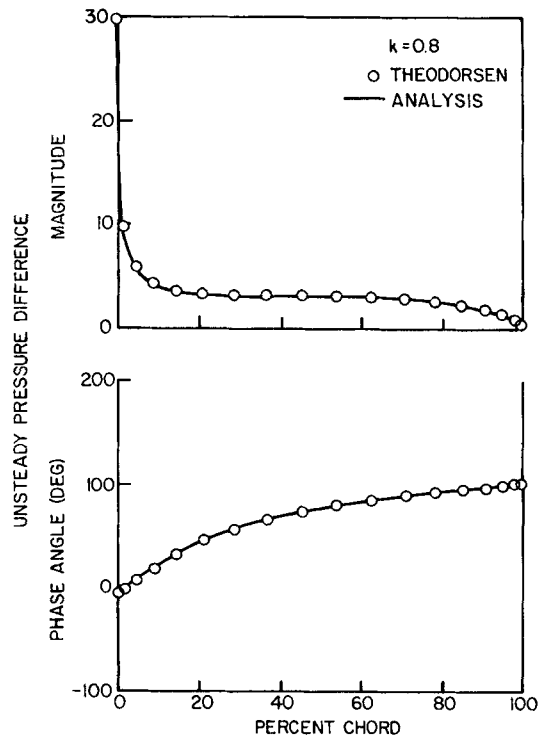

Figure 5. Correlation of locally analytic prediction and classical solution for an oscillating flat plate

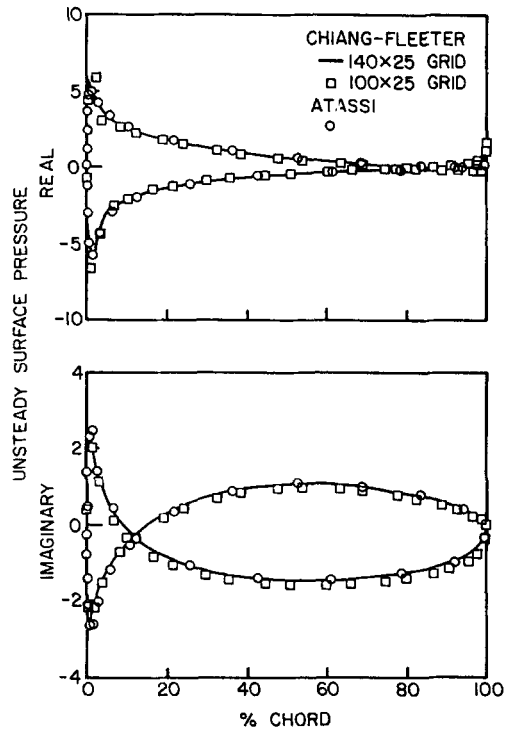

Figure 6. Locally analytic prediction correlation and grid refinement for an 11·25% thick, 3·5% camber, Joukowski aerofoil

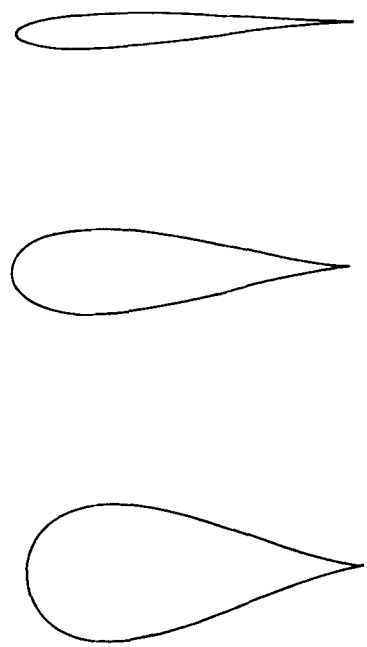

Figure 7. Joukowski aerofoils with 10%, 25% and 40% thickness-to-chord ratios

The predicted chordwise distributions of the steady velocity on the surfaces of the Joukowski and flat plate aerofoils are presented in Figure 8. The velocity distributions are symmetric on the aerofoil surfaces, as expected, with the aerofoil thickness resulting in a chordwise gradient in the surface velocity. The maximum steady velocity on the surfaces is located near the front of the aerofoil, but moves rearward as the thickness increases.

The predicted chordwise distributions of the complex unsteady pressure on the surfaces of the oscillating aerofoils are presented in Figure 9 with the thickness-to-chord ratio as parameter. Analogous to the steady results, the unsteady pressure distributions are symmetric on the aerofoil surfaces, with the aerofoil thickness primarily affecting the unsteady surface pressure over the front portion of the aerofoil. Also, the maximum value of the real and imaginary parts of the unsteady surface pressure moves rearward with increasing thickness.

To demonstrate more clearly the effect of aerofoil thickness on the unsteady aerodynamics, the complex unsteady pressure differences across the chordline of the aerofoil are calculated and presented in a magnitude and phase angle format in Figure 10. Both the phase angle and the magnitude of the unsteady pressure difference are dependent on the aerofoil thickness. As the thickness-to-chord ratio increases, the pressure difference phase angle decreases over the front 40% of the chord and increases over the rear 60% of the chord. The maximum magnitude of the unsteady pressure difference decreases with increasing thickness-to-chord ratio and also moves aft on the aerofoil.

Camber effects

Figure 11 shows the three Joukowski aerofoils utilized to investigate the effects of aerofoil camber. These aerofoils have 10%, 15%, and 20% camber, with each having a thickness-to-chord ratio of 20%. Also considered is the flat plate aerofoil as a reference.

The predicted chordwise steady velocity distributions are presented in Figure 12. For non-zero camber, the velocities on the aerofoil surfaces become non-symmetric, as expected. As the camber increases, the velocity increases on the upper surface and decreases on the lower surface.

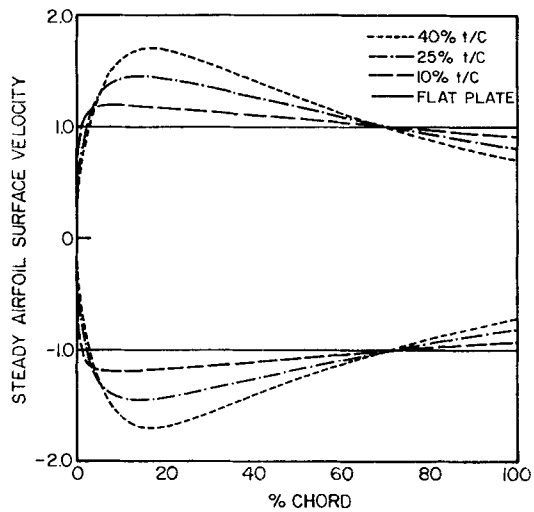

Figure 8. Effect of thickness-to-chord ratio on the aerofoil surface steady velocity

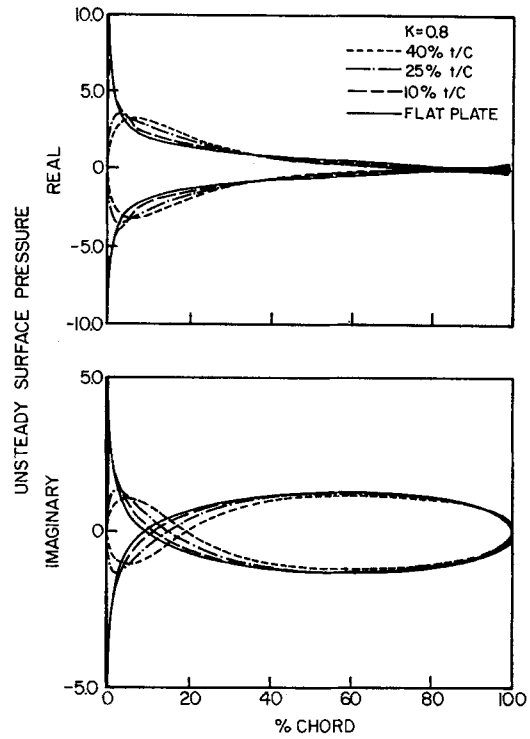

Figure 9. Variation of the unsteady surface pressure distribution with thickness-to-chord ratio

Figures 13 and 14 present the predicted chordwise distributions of the complex unsteady pressure on the oscillating aerofoil surfaces and the unsteady pressure differences across the chordline of the aerofoil, respectively, with camber as parameter. In the leading-edge region the cambered aerofoil results differ from the flat plate results but are in relative agreement with one another. Aft of the leading-edge region, increasing the camber results in a decrease in the magnitude of the unsteady pressure difference. The phase angle of the pressure difference decreases with increasing camber forward of 55% chord and increases aft of this chord location.

Mean flow incidence effects

Figure 15 depicts a Joukowski aerofoil with a 20% thickness-to-chord ratio and 5% camber at mean flow incidence angle values of 0°, 5° and 10°. The predicted aerofoil surface chordwise steady velocity distributions presented in Figure 16 are non-symmetric. As the incidence angle increases, the steady surface velocity increases on the upper surface and decreases on the lower surface, with the largest incidence effects being found over the front portion of the aerofoil.

The complex unsteady pressure distributions on the aerofoil surfaces with incidence angle as parameter are presented in Figure 17. These distributions are a function of the incidence angle, with the largest effects apparent over the front portion of the aerofoil, analogous to the steady results.

The unsteady pressure difference across the chordline of the aerofoil as a function of the mean flow incidence angle is shown in Figure 18. The phase lag is nearly independent of the incidence angle. However, the magnitude of the unsteady pressure difference is dependent on the incidence angle, with the largest effects found over the front portion of the aerofoil, analogous to the steady

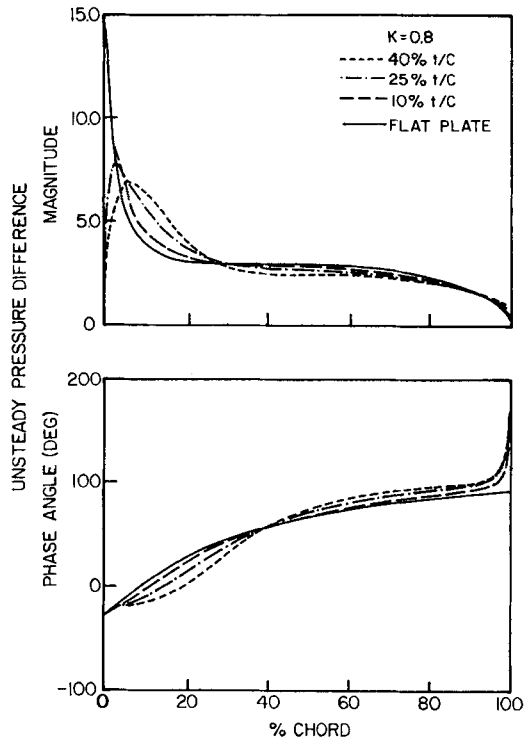

Figure 10. Variation of the unsteady pressure difference across the aerofoil chordline with thickness-to-chord ratio

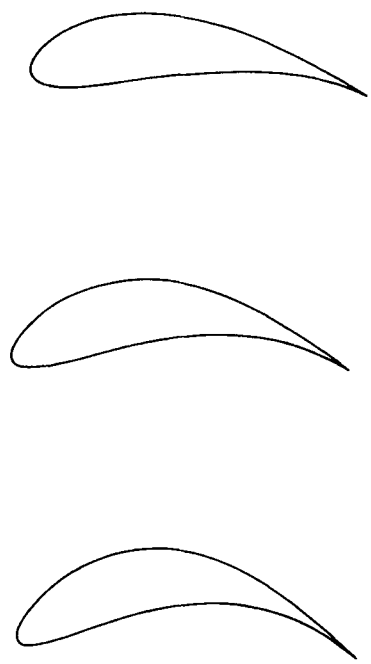

Figure 11. Joukowski aerofoils with 10%, 15% and 20% camber

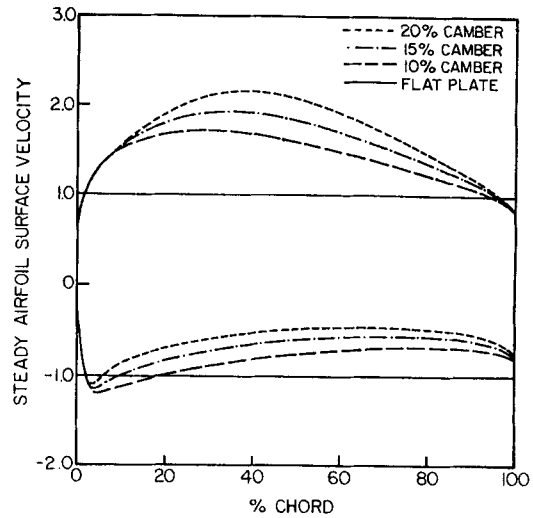

Figure 12. Effect of aerofoil camber on the aerofoil surface steady velocity

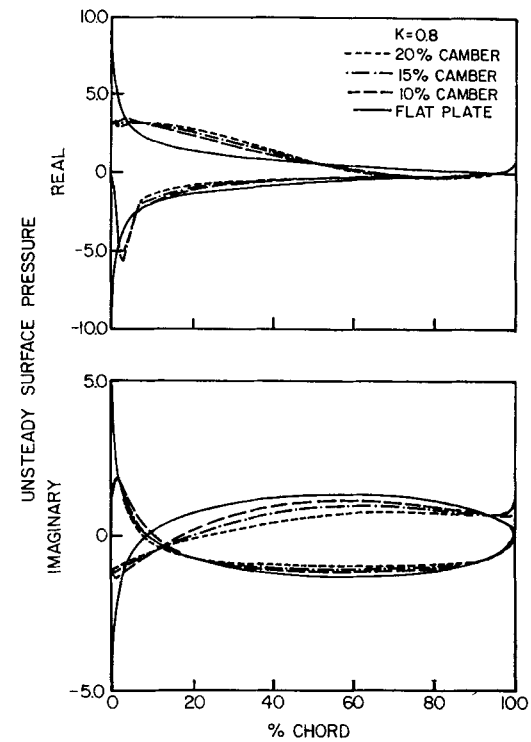

Figure 13. Variation of the unsteady surface pressure distribution with aerofoil camber

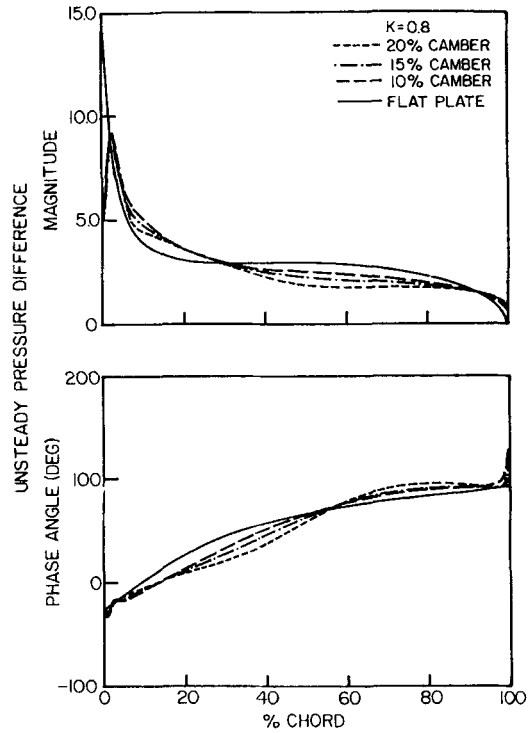

Figure 14. Variation of the unsteady pressure difference across the aerofoil chordline with aerofoil camber

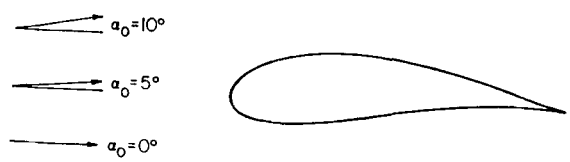

Figure 15. A Joukowski aerofoil at mean flow incidence angles of 0°, 5° and 10°

results. Also, as the incidence is increased, the magnitude of the unsteady pressure difference decreases over the front portion of the aerofoil, becoming nearly independent of the incidence angle aft of approximately the 25% chord location.

CONCLUSIONS

A complete first-order model and locally analytic solution method have been developed to analyse the effects of mean flow incidence and aerofoil camber and thickness on the incompressible aerodynamics of an oscillating aerofoil. This method incorporates analytic solutions, with the discrete algebraic equations which represent the differential flow field equations obtained from analytic solutions in individual grid elements. The complete flow field solution is then obtained by assembling these locally analytic solutions.

The velocity potential was separated into steady and unsteady harmonic parts, with the unsteady potential further decomposed into circulatory and non-circulatory components. The

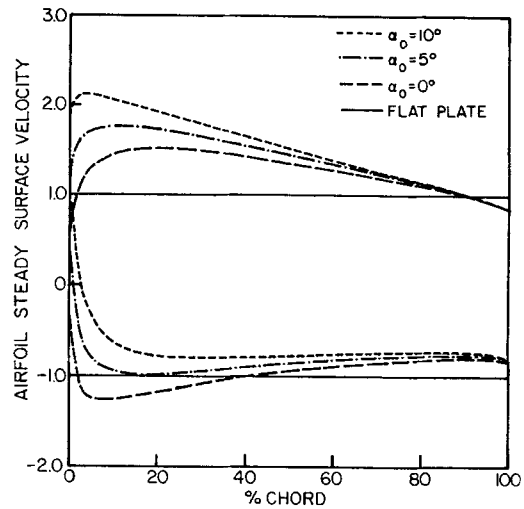

Figure 16. Effect of mean flow incidence angle on the aerofoil surface steady velocity

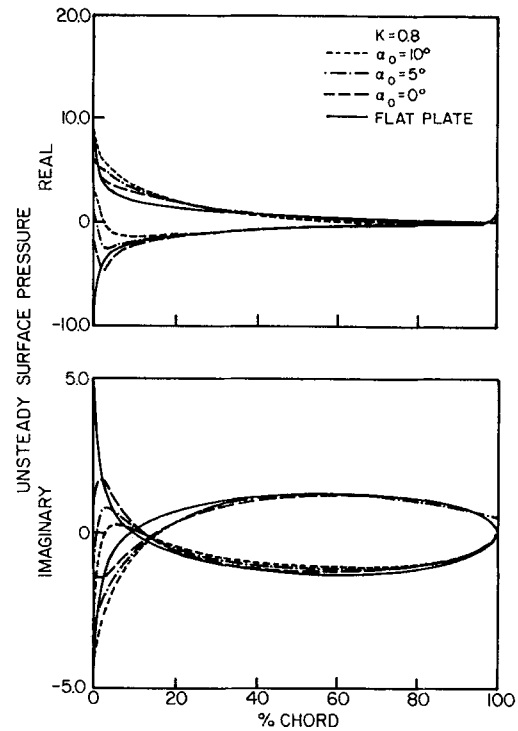

Figure 17. Variation of the unsteady surface pressure distribution with mean flow incidence angle

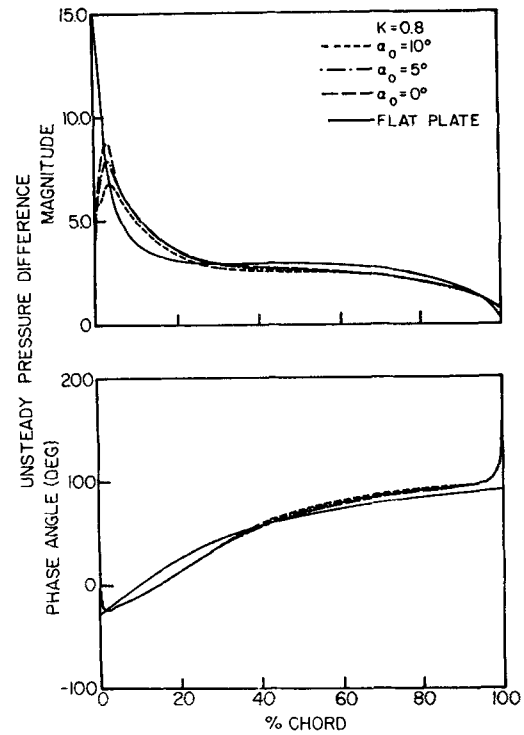

Figure 18. Variation of the unsteady pressure difference across the aerofoil chordline with mean flow incidence angle

steady velocity potential is independent of the unsteady flow field. However, the unsteady flow is coupled to the steady flow field through the boundary conditions on the oscillating aerofoil.

This model and solution method were shown to accurately predict the Theodorsen oscillating flat plate classical solution. Locally analytic solutions for a series of Joukowski aerofoils demonstrated the strong coupling between the aerofoil unsteady and steady flow fields, i.e. the strong dependence of the oscillating aerofoil aerodynamics on the steady flow effects of mean flow incidence and aerofoil camber and thickness.

ACKNOWLEDGEMENTS

This research was sponsored in part by both the Air Force Office of Scientific Research and the NASA Lewis Research Center.

NOMENCLATURE

b	aerofoil semi-chord, $C/2$
k	reduced frequency, $\omega b/U_\infty$
U_0	steady chordwise velocity component
V_0	steady normal velocity component
U_∞	far-field steady chordwise velocity component
V_∞	far-field steady normal velocity component
W'	upwash on aerofoil

X non-dimensional chordwise co-ordinate, X/b
X_0 elastic axis location
Y non-dimensional normal co-ordinate, Y/b
ξ transformed chordwise co-ordinate
η transformed normal co-ordinate
Φ general velocity potential
α_0 mean incidence angle
Φ_0 steady velocity potential
Φ' unsteady velocity potential
Φ'_C circulatory unsteady velocity potential
Φ'_{NC} non-circulatory unsteady velocity potential
$\bar{\Phi}$ shorthand representation for velocity potential Φ_0, Φ'_{NC} or Φ'_C
Γ steady circulation constant
Γ' unsteady circulation constant
P' unsteady pressure
ω oscillatory frequency
$\bar{\alpha}$ amplitude of torsional oscillations

Superscripts

$+$ upper surface
$-$ lower surface

REFERENCES

1. J. H. Horlock, 'Fluctuating lift forces on airfoils moving through transverse and cordwise gusts', *ASME J. Basic Eng. Series D*, **90** (4), 494–500 (December 1968).
2. W. R. Sears, 'Some aspects of nonstationary airfoil theory and its practical applications', *J. Aeronaut. Sci.*, **8** (3), 104–108 (January 1941).
3. H. Naumann and H. Yeh, 'Lift and pressure fluctuations of a cambered airfoil under periodic gusts and applications to turbomachinery', *ASME Paper 72-GT-30*, 1972.
4. M. E. Goldstein and H. Atassi, 'A complete second order theory for the unsteady flow about an airfoil due to a periodic gust', *J. Fluid Mech.*, **74**, 741–766 (1976).
5. H. Atassi and T. J. Akai, 'Aerodynamic and aeroelastic characteristics of oscillating loaded cascades at low Mach number', *ASME Paper 79-GT-111*, 1979.
6. J. R. Spreiter and A. Y. Alksne, 'Thin airfoil theory based on approximate solution of the transonic flow equation', *NACA-TR-1359*, 1958.
7. J. R. Spreiter, 'Aerodynamics of wings and bodies at transonic speeds', *J. Aerospace Sci.*, **26** (8), 465–487 (August 1959).
8. J. R. Spreiter, 'The local linearization method in transonic flow theory', in K. Oswatitsch (ed.), *Symp. Transsonicum*, Springer-Verlag, Berlin, Göttingen, Heidelberg, 1964, pp. 92–109.
9. S. S. Stahara and J. R. Spreiter, 'Development of a nonlinear unsteady transonic flow theory' *NASA-CR-2258*, June 1973.
10. E. H. Dowell, 'A simplified theory of oscillating airfoils in transonic flow', in R. B. Kinney (ed.), *Proc. Symp. on Unsteady Aerodynamics*, University of Arizona, Tucson, July 1975, pp. 655–679.
11. C. J. Chen, H. Naseri-Neshat and K. S. Ho, 'Finite analytic numerical solution of heat transfer in two-dimensional cavity flow', *J. Numer. Heat Transfer*, **4**, 179–197 (1981).
12. C. J. Chen and Y. H. Yoon, 'Finite analytic numerical solution of axisymmetric Navier–Stokes and energy equations', *J. Heat Transfer*, **5**, 639–645 (August 1983).
13. C. J. Chen and P. Li, 'Finite differential methods in heat conduction—application of analytic solution techniques', *ASME Paper 79-WA/HT-50*, December 1979.
14. C. J. Chen and P. Li, 'The finite analytic method for steady and unsteady heat transfer problems', *ASME Paper 80-HT-86*, 1980.
15. J. F. Thompson, F. C. Thames and C. W. Mastin, 'Boundary fitted curvilinear coordinate systems for solution of partial differential equations on fields containing any number of arbitrary two-dimensional bodies', *NASA-CR 2729*, 1977.
16. T. Theodorsen, 'General theory of aerodynamic instability and the mechanism of flutter', *NACA-TR-496*, 1935.